

Turb-L1: Achieving Long-term Turbulence Tracing By Tackling Spectral Bias

Hao Wu^{1,*}, Yuan Gao^{1,*}, Ruiqi Shu^{1,*}, Zean Han^{2,3}, Fan Xu⁴,
Zhihong Zhu^{5,6}, Qingsong Wen⁷, Xian Wu⁵, Kun Wang^{8,†}, Xiaomeng Huang^{1,†}

¹Tsinghua University, ²The Hong Kong University of Science and Technology,

³The Chinese University of Hong Kong, ⁴University of Science and Technology of China,

⁵Tencent, ⁶Peking University, ⁷Squirrel Ai Learning, ⁸Nanyang Technological University
wk520529wjh@gmail.com, hxm@tsinghua.edu.cn

Abstract

Accurately predicting the long-term evolution of turbulence is crucial for advancing scientific understanding and optimizing engineering applications. However, existing deep learning methods face significant bottlenecks in long-term autoregressive prediction, which exhibit excessive *smoothing* and fail to accurately track complex fluid dynamics. Our extensive experimental and spectral analysis of prevailing methods provides an interpretable explanation for this shortcoming, identifying **Spectral Bias** as the core obstacle. Concretely, spectral bias is the inherent tendency of models to favor low-frequency, smooth features while overlooking critical high-frequency details during training, thus reducing fidelity and causing physical distortions in long-term predictions. Building on this insight, we propose **Turb-L1**, an innovative turbulence prediction method, which utilizes a Hierarchical Dynamics Synthesis mechanism within a multi-grid architecture to explicitly overcome spectral bias. It accurately captures cross-scale interactions and preserves the fidelity of high-frequency dynamics, enabling reliable long-term tracking of turbulence evolution. Extensive experiments on the 2D turbulence benchmark show that **Turb-L1** demonstrates excellent performance: **(I)** In long-term predictions, it reduces Mean Squared Error (MSE) by 80.3% and increases Structural Similarity (SSIM) by over $9\times$ compared to the SOTA baseline, significantly improving prediction fidelity. **(II)** It effectively overcomes spectral bias, accurately reproducing the full enstrophy spectrum and maintaining physical realism in high-wavenumber regions, thus avoiding the spectral distortions or spurious energy accumulation seen in other methods. **(III)** It achieves outstanding long-term stability with a relative L2 error as low as 0.444, substantially outperforming baseline methods and proving its robustness. Our codes are available at https://github.com/easylearningscores/TurbL1_AI4Science.

1 Introduction

Turbulence [39, 47, 5, 7], the intricate and chaotic dance of fluids shaping phenomena from weather systems to aerodynamic efficiency [2, 18, 46, 9]. Accurate prediction of its long-term evolution is paramount not only for fundamental scientific understanding in fields like astrophysics [4] and climate modeling [13, 50, 38] but also for critical engineering applications such as optimizing energy conversion [32, 3] and reducing drag [15, 14]. However, its inherent multiscale nature [16, 17], characterized by strong nonlinearity [27, 26], chaotic dynamics, and the crucial energy cascade across

*These authors contributed equally.

†Corresponding authors.

scales, where fine structures dictate macroscopic behavior, renders long-term, high-fidelity prediction an enduring scientific frontier [25, 7, 8, 43, 42].

Traditional numerical simulations for fluid dynamics, such as direct numerical simulation (DNS) [25, 36, 19], large eddy simulation (LES) [51, 31], and Reynolds average Navier-Stokes (RANS) models [1, 10], while foundational, grapple with a persistent trade-off between *computational cost* and *physical accuracy*, particularly hindering long-duration, high-resolution turbulence modeling. This challenge spurred interest in deep learning, which, despite successes in tasks like reconstruction [41, 21] and short-term forecasting [23, 20, 46], encounters a critical and widespread limitation when applied to the demanding problem of long-term autoregressive turbulence prediction using current mainstream architectures (e.g., Convolutional neural networks (CNNs) [11], Transformers [45], Neural Operators [49, 20]). Inherent architectural characteristics, such as resolution loss in CNNs, difficulty capturing localized high-frequencies in Transformers, or explicit/implicit filtering in Operators—often lead to a failure to preserve crucial fine-scale dynamics. Consequently, while initial predictions may seem plausible, extended rollouts rapidly diverge from physical reality, manifesting as excessive smoothing, loss of vital vortex structures, severe energy spectrum distortions, and unphysical artifacts, as shown in Figure. 1a, ultimately undermining their reliability for long-range forecasting needs that traditional methods also struggled to meet efficiently.

This study delves into the fundamental reasons underpinning this prevalent failure across diverse deep learning architectures. We identify and argue that the core issue stems from an inherent property of many standard models: spectral bias [33]. This bias manifests as a tendency during training to preferentially learn smooth, large-scale, low-frequency components, while struggling to accurately capture and maintain the less energetic, yet dynamically critical, high-frequency, small-scale structures. For turbulence, whose very essence lies in the intricate cross-scale energy cascade and the dynamics of fine-scale vortices governing dissipation, this inherent learning preference is particularly destructive. It leads models to systematically neglect or misrepresent the behavior of these vital high-frequency components, disrupting the proper energy transfer across scales. As a direct consequence, even small initial errors, particularly in the poorly learned high-frequency range, rapidly amplify during the autoregressive prediction process within the nonlinear system. This amplification directly leads to the observed degradation of fine structures and emergence of artifacts seen visually (Figure. 1a), manifests as anomalous high-wavenumber energy behavior and severe spectral distortions (Figure. 1b), and ultimately hinders the ability to accurately trace the turbulence evolution over extended periods.

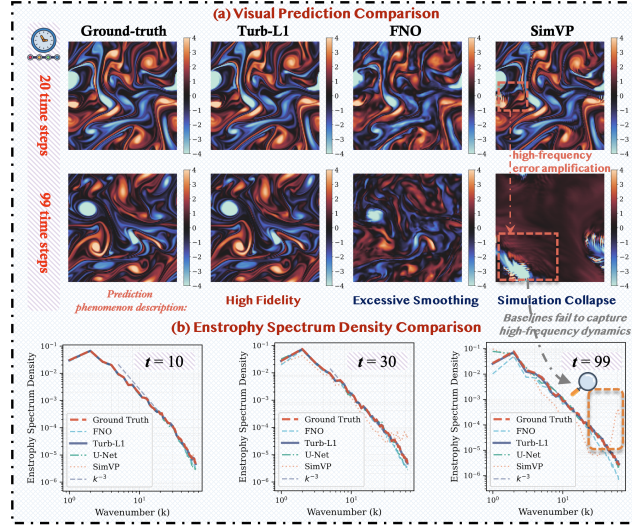


Figure 1: Long-term turbulence prediction performance comparison. (a) Visual comparison of vorticity fields ($t=20$, $t=99$). Turb-L1 maintains high fidelity to the Ground-truth, while baselines exhibit excessive smoothing (e.g., FNO) or simulation collapse with artifacts (e.g., SimVP) driven by high-frequency error amplification. **(b)** Entrophy spectrum density comparison ($t=10$, 30 , 99). Baselines fail to capture high-frequency dynamics, increasingly deviating from the Ground Truth at high wavenumbers (k) over time, whereas Turb-L1 accurately preserves spectral characteristics.

💡 *How then can we fundamentally improve prediction if inherent spectral bias prevents accurately tracing turbulence long-term? This work demonstrates a path forward by **tackling** what we identify as a **spectral bias**, thereby **achieving** reliable **long-term turbulence tracing**.*

Addressing the limitations of existing deep learning methods often compromised by spectral bias in long-term turbulence forecasting, this paper presents Turb-L1. Crucially, the design of Turb-L1 is

directly motivated by our interpretable identification of spectral bias as the primary impediment to accurate long-term prediction. Our method stems from a more foundational principle: learning the intrinsic spectral dynamics across interacting scales. To this end, we introduce the Hierarchical Dynamics Synthesis mechanism within a multi-grid framework (Figure 2). This process first employs operators highly sensitive to local, high-frequency variations to capture fine-grained turbulent features; subsequently, it utilizes mechanisms adept at global context integration to model the evolution of large-scale structures and their coupling with finer scales. Through the careful orchestration of this two-stage synergistic spectral feature synthesis process, explicit refining of high-frequency components before their integration into the global context, **Turb-L1** effectively captures the complex cross-scale energy transfer fundamental to turbulence. As demonstrated visually and spectrally in Figure 1, unlike baseline methods that succumb to excessive smoothing or simulation collapse, our approach preserves high-fidelity details and maintains physical consistency over extended rollouts. This design enables robust and accurate long-range predictions crucial for scientific and engineering applications. We conducted extensive experiments on challenging turbulence benchmarks, where **Turb-L1** achieves consistent state-of-the-art (SOTA) performance, demonstrating significant gains in long-term fidelity and stability.

Experimental Observations. Comparative experiments on the McWilliams 2D turbulence benchmark [24] validate the effectiveness of **Turb-L1**. **① Delivers state-of-the-art long-term accuracy and fidelity:** At $t = 99$, **Turb-L1** reduces MSE to 0.617, an 80.3% improvement over the best baseline FNO, and maintains SSIM at 0.682, over $9\times$ higher than baselines like FNO, SimVP, and UNet, successfully preserving fine-scale structures. **② Overcomes spectral bias, maintaining physical realism:** As shown in Figure 1b, it accurately captures the full enstrophy spectrum, crucially preserving high-frequency dynamics. This avoids issues like the excessive smoothing seen in FNO or the error explosion leading to simulation collapse observed in SimVP, where MSE increased over $14\times$ from $t = 20$ to $t = 99$. **③ Exhibits superior long-term stability:** At $t = 99$, the relative L2 error is only 0.444. This is at least 57% lower than baselines typically exceeding 1.0, such as FNO at 1.041 and SimVP at 1.321. This ensures reliable tracking of turbulence dynamics, highlighting its significant potential for long-term scientific and engineering prediction tasks.

To the best of our knowledge, **Turb-L1** represents the first systematic study addressing long-term modeling in turbulent scenarios. We summarize our key contributions as follows: \blacktriangleright We establish spectral bias as a critical, interpretable factor limiting current deep learning approaches in long-term turbulence predictions. \blacktriangleright We introduce **Turb-L1**, a novel method designed to explicitly counteract this bias, thereby enabling unprecedented long-term prediction fidelity and physical realism. \blacktriangleright Comprehensive validation demonstrating **Turb-L1**’s state-of-the-art long-term prediction capabilities.

2 Method

2.1 Problem Definition

Forecasting the spatiotemporal evolution of turbulence, a complex fluid dynamic phenomenon governed by the Navier-Stokes equations and often characterized by its vorticity field $\omega(\mathbf{x}, t)$ in 2D incompressible flows, remains a significant challenge. The dynamics of $\omega(\mathbf{x}, t)$ are described by the vorticity transport equation, often written in conservative form for incompressible flow ($\nabla \cdot \mathbf{u} = 0$):

$$\frac{\partial \omega(\mathbf{x}, t)}{\partial t} + \nabla \cdot (\mathbf{u}(\mathbf{x}, t) \omega(\mathbf{x}, t)) = \nu \nabla^2 \omega(\mathbf{x}, t) + f(\mathbf{x}, t) \quad (1)$$

where $\mathbf{u}(\mathbf{x}, t)$ is the velocity field, ν denotes kinematic viscosity, and $f(\mathbf{x}, t)$ represents external forcing. Our objective is to develop a deep learning surrogate model, parameterized by θ , denoted as $\mathcal{F}(\cdot; \theta)$, which approximates the solution operator for long-term autoregressive forecasting. Given an initial state $\omega_0(\mathbf{x}) = \omega(\mathbf{x}, t_0)$, the model iteratively predicts future vorticity states:

$$\hat{\omega}(\mathbf{x}, t_{k+1}) = \mathcal{F}(\hat{\omega}(\mathbf{x}, t_k); \theta) \quad (2)$$

where $t_{k+1} = t_k + \Delta t$. The primary challenge is maintaining long-term high-fidelity and physical realism, especially in capturing crucial multi-scale interactions and high-frequency details often compromised by spectral bias in current learning architectures.

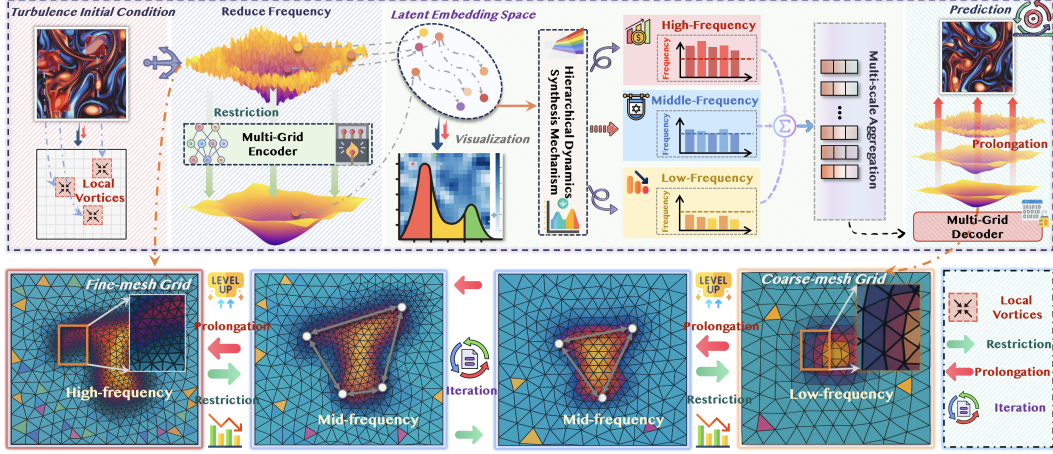


Figure 2: Overview of the **Turb-L1** architecture. The model initially downscales the turbulence initial condition and embeds it into a latent space via a multi-grid encoder (\mathcal{E}). The core **Hierarchical Dynamics Synthesis Mechanism** (\mathcal{HDS}) then explicitly synthesizes dynamical features across different frequencies (high ω_H , middle ω_M , and low ω_L) within this latent space. Subsequently, multi-scale aggregated features are upsampled by a multi-grid decoder (\mathcal{D}), ultimately generating high-fidelity turbulence predictions. The lower panel details the multi-grid operations—Restriction (\mathcal{R}), Prolongation (\mathcal{P}), and Iteration (\mathcal{I})—illustrating how the model processes and transfers information across various grid scales to effectively capture cross-scale interactions and overcome spectral bias.

2.2 Overview of the Proposed Method: Turb-L1

To approximate the turbulence solution operator $\mathcal{F}(\cdot; \theta)$ (Eq. 2) and mitigate spectral bias for long-term high-fidelity forecasting, we introduce **Turb-L1**, as shown in Figure 2. This framework transforms an input vorticity field $\omega(\mathbf{x}, t_k)$ (or a history thereof) into a predicted state $\hat{\omega}(\mathbf{x}, t_{k+1})$ through a meticulously designed sequence of learnable operators. **Turb-L1** first employs a multi-grid encoder \mathcal{E} to extract hierarchical latent features, followed by a core Hierarchical Dynamics Synthesis mechanism \mathcal{HDS} that evolves these features while preserving cross-spectral fidelity, and finally a multi-grid decoder \mathcal{D} to reconstruct the output. This composite mapping, critical for robust autoregressive prediction, is denoted as:

$$\hat{\omega}(\mathbf{x}, t_{k+1}) = (\mathcal{D} \circ \mathcal{HDS} \circ \mathcal{E})(\omega(\mathbf{x}, t_k); \theta) \equiv \mathcal{F}(\omega(\mathbf{x}, t_k); \theta) \quad (3)$$

where θ are all learnable parameters $\{\theta_{\mathcal{E}}, \theta_{\mathcal{HDS}}, \theta_{\mathcal{D}}\}$, and for $k > 0$, $\omega(\mathbf{x}, t_k)$ becomes $\hat{\omega}(\mathbf{x}, t_k)$.

2.3 Projecting Turbulence onto a Latent Manifold Space

The initial stage of **Turb-L1** involves the Multi-Grid Encoder, $\mathcal{E}(\cdot; \theta_{\mathcal{E}})$, transforming the high-dimensional input vorticity field $\omega(\mathbf{x}, t_k)$ into a structured, multi-scale latent representation. Turbulent flows, rich in high-frequency, small-scale structures, pose challenges for direct processing.

Inspired by multi-grid methods, our encoder \mathcal{E} hierarchically projects data onto a latent manifold \mathcal{M}_{ω} where dynamics are assumed to be smoother. This involves restriction operators \mathcal{R}_l and learned transformations $\phi_l(\cdot; \theta_{\mathcal{E}}^{(l)})$. The restriction operator \mathcal{R}_l , as shown in Figure 2, Restriction, showing higher information density to a coarser grid via local aggregation or pooling. This crucial step reduces dimensionality and acts as a localized filter, preferentially passing smoother, large-scale signal components to coarser levels. The learned transformations ϕ_l then process these restricted features:

$$\mathbf{z}^{(0)}(\mathbf{x}, t_k) = \phi_0(\omega(\mathbf{x}, t_k); \theta_{\mathcal{E}}^{(0)}) \quad (4)$$

$$\mathbf{z}^{(l+1)}(\mathbf{x}', t_k) = \phi_{l+1}(\mathcal{R}_l(\mathbf{z}^{(l)}(\mathbf{x}, t_k)); \theta_{\mathcal{E}}^{(l+1)}), \quad \text{for } l = 0, \dots, L-1 \quad (5)$$

where $\mathbf{z}^{(l)}$ is the latent representation at grid level l . This multi-grid encoding hierarchically disentangles features for effective cross-scale modeling, enhances computational efficiency, and facilitates dynamics learning on smoother latent manifolds by mitigating the stiffness and high dimensionality of the original PDE solution space, thus providing a rich, multi-scale context for the HDS mechanism.

2.4 Hierarchical Dynamics Synthesis for Full-Spectrum Fidelity

The Hierarchical Dynamics Synthesis (HDS) mechanism, $\mathcal{HDS}(\cdot; \theta_{\mathcal{HDS}})$, is pivotal to **Turb-L1**'s strategy for mitigating spectral bias. It operates on the latent representation $\mathbf{z}_{\text{enc}} \in \mathcal{M}_\omega$ from the multi-grid encoder \mathcal{E} , precisely evolving turbulence dynamics within this manifold. The HDS design leverages insights into the distinct frequency responses of neural operators: Convolutional Neural Networks (CNNs) excel at capturing high-frequency local details, whereas Transformer-like architectures are adept at integrating low-frequency global information [28, 22]. **Turb-L1** architecturally synergizes these complementary properties for precise, high-fidelity, full-spectrum turbulence evolution.

Models reliant on a single operator type often exhibit spectral bias, prioritizing high-energy, low-frequency components over crucial high-frequency fine structures in turbulence. To counter this, HDS employs a heterogeneous, multi-path dynamics feature synthesis framework (Figure 2, center), departing from homogeneous evolution. This framework concurrently processes \mathbf{z}_{enc} to extract and evolve features across distinct frequency scales. For each band ω_s ($s \in \{H, M, L\}$ for high, middle, low), a tailored non-linear transformation $\mathcal{T}_{\omega_s}(\cdot; \theta_{\mathcal{HDS}}^{(s)})$ generates dynamic primitives \mathbf{h}_{ω_s} :

$$\mathbf{h}_{\omega_s} = \mathcal{T}_{\omega_s}(\mathbf{z}_{\text{enc}}; \theta_{\mathcal{HDS}}^{(s)}). \quad (6)$$

The specific architecture of each \mathcal{T}_{ω_s} is optimized for its designated frequency band.

For synthesizing *high-frequency dynamic primitives* \mathbf{h}_{ω_H} , \mathcal{T}_{ω_H} employs operators highly sensitive to local variations and high-frequency content. Convolutional operations, particularly with small receptive field kernels $\kappa_j^{(H)}$, inherently function as high-pass filters, adept at extracting high-frequency signals such as edges and textures. Consequently, \mathcal{T}_{ω_H} is primarily instantiated via such convolutional architectures:

$$[\mathcal{T}_{\omega_H}(\mathbf{z}_{\text{enc}})](\mathbf{x}') = \sigma \left(\sum_j \int_{\mathcal{N}(\mathbf{x}')} \kappa_j^{(H)}(\mathbf{x}' - \mathbf{y}') \mathbf{z}_{\text{enc}}(\mathbf{y}') d\mathbf{y}' + \mathbf{b}_j^{(H)} \right), \quad (7)$$

where σ is an activation and $\mathbf{b}_j^{(H)}$ a bias. This design is aimed at enhancing gradient-like information and fine vortex features within \mathbf{z}_{enc} .

Conversely, synthesizing *low-frequency dynamic primitives* \mathbf{h}_{ω_L} is achieved by \mathcal{T}_{ω_L} , which targets large-scale structures and global flow trends. The self-attention mechanism (MSA) in Transformers, by performing a weighted average across all input elements, inherently acts as a low-pass filter, effectively integrating global context. \mathcal{T}_{ω_L} is thus instantiable as a Global Adaptive Weighted Aggregation (GAWA) mechanism, rooted in MSA:

$$[\mathcal{T}_{\omega_L}(\mathbf{z}_{\text{enc}})]_i = \sum_{k=1}^{N_h} \mathbf{W}_k^{(O)} \left(\sum_{j=1}^{N_T} \alpha_{ij}^{(k)} (\mathbf{W}_k^{(V)} \mathbf{z}_j) \right), \quad (8)$$

where $\alpha_{ij}^{(k)} = \text{softmax}_j \left(\frac{(\mathbf{W}_k^{(Q)} \mathbf{z}_i)^T (\mathbf{W}_k^{(K)} \mathbf{z}_j)}{\sqrt{d_k}} \right)$, N_T is the token count, and $\mathbf{W}_k^{(\cdot)}$ are learnable head projection matrices.

The concurrently generated dynamic primitives $\{\mathbf{h}_{\omega_H}, \mathbf{h}_{\omega_M}, \mathbf{h}_{\omega_L}\}$, conveying distinct frequency channel information, are subsequently fused by a Multi-scale Dynamic Aggregation (MDA) module, $\mathcal{A}_{\text{MDA}}(\cdot, \cdot, \cdot; \theta_{\mathcal{HDS}}^{(\text{agg})})$. Realized as a sequence of convolutional blocks, \mathcal{A}_{MDA} learns to effectively combine these multi-frequency features, capturing their non-linear dependencies and facilitating cross-frequency interactions. This process yields a unified latent representation $\mathbf{z}_{\text{HDS_out}}$ encapsulating the full-spectrum evolved dynamics:

$$\mathbf{z}_{\text{HDS_out}} = \mathcal{A}_{\text{MDA}}(\mathbf{h}_{\omega_H}, \mathbf{h}_{\omega_M}, \mathbf{h}_{\omega_L}; \theta_{\mathcal{HDS}}^{(\text{agg})}). \quad (9)$$

As depicted in Figure 2, the HDS output $\mathbf{z}_{\text{HDS_out}}$ is subsequently channeled to the multi-grid decoder \mathcal{D} . The core HDS strategy, involving explicit extraction of frequency-specific dynamics, their dedicated processing, and intelligent aggregation via the convolutional MDA in latent space, forces the model to learn and preserve critical high-frequency details. By accurately capturing global flow while maintaining these fine structures, this design fundamentally mitigates spectral bias, enabling **Turb-L1** to trace complex, multi-scale turbulence evolution with high fidelity.

2.5 Mapping to Physical Space

The Multi-Grid Decoder \mathcal{D} receives the latent space features $\mathbf{z}_{\text{HDS_out}}$, evolved by the HDS module. Through a sequence of sophisticated hierarchical operations, it aims to reconstruct the turbulent vorticity field $\hat{\omega}(\mathbf{x}, t_{k+1})$ in the physical space with maximal fidelity. This process initiates from the coarsest latent representation (corresponding to $\mathbf{z}_{\text{HDS_out}}$). It iteratively applies a Prolongation Operator \mathcal{P}_l (upsampling features from level $l + 1$ to l) followed by a learnable Feature Refinement Module $\psi_l(\cdot; \theta_{\mathcal{D}}^{(l)})$ (refining features at level l). This nested sequence of composite operations, where l ranges from $L - 1$ down to 0, progressively restores the latent representation. Finally, an output transformation layer $\mathcal{T}_{\text{out}}(\cdot; \theta_{\mathcal{D}}^{(\text{out})})$ maps this fully refined fine-level representation to the final vorticity field prediction. The synergy between the decoder and the HDS mechanism ensures the effective reproduction of full-spectrum dynamical information, particularly high-frequency fine structures, thereby achieving high-fidelity and physically consistent tracking of turbulence evolution. Its overall mathematical formulation is:

$$\hat{\omega}(\mathbf{x}, t_{k+1}) = \mathcal{T}_{\text{out}} \left(\psi_0 \left(\mathcal{P}_0 \left(\dots \psi_{L-1} \left(\mathcal{P}_{L-1} (\mathbf{z}_{\text{HDS_out}}); \theta_{\mathcal{D}}^{(L-1)} \right) \dots \right); \theta_{\mathcal{D}}^{(0)} \right); \theta_{\mathcal{D}}^{(\text{out})} \right) \quad (10)$$

where $\mathbf{z}_{\text{HDS_out}}$ is the output from the HDS module, \mathcal{P}_l denotes the Prolongation operator at stage l , $\psi_l(\cdot; \theta_{\mathcal{D}}^{(l)})$ is the Feature Refinement Module with parameters $\theta_{\mathcal{D}}^{(l)}$ for stage l (operating on the output of \mathcal{P}_l), and $\mathcal{T}_{\text{out}}(\cdot; \theta_{\mathcal{D}}^{(\text{out})})$ is the final output transformation layer with parameters $\theta_{\mathcal{D}}^{(\text{out})}$. The ‘...’ indicates the continuation of the nested application of $(\psi \circ \mathcal{P})$ blocks for intermediate stages.

We theoretically analyze the link between a model’s spectral accuracy, particularly for high-frequency components, and its long-term autoregressive stability. Consider the true state evolution $\omega(t_{k+1}) = S(\omega(t_k))$ and its model approximation $\hat{\omega}(t_{k+1}) = \mathcal{F}(\hat{\omega}(t_k))$. The prediction error $\epsilon(t_k) = \hat{\omega}(t_k) - \omega^*(t_k)$ evolves approximately as:

$$\epsilon(t_{k+1}) \approx \mathbf{A}_k \epsilon(t_k) + \mathbf{e}_{\text{model}}(t_k), \quad (11)$$

where $\mathbf{A}_k = \nabla S|_{\omega^*(t_k)}$ is the system Jacobian and $\mathbf{e}_{\text{model}}(t_k) = \mathcal{F}(\omega^*(t_k)) - S(\omega^*(t_k))$ is the single-step model error. Let \mathbf{P}_{high} be the projection operator onto a high-frequency subspace.

Theorem 2.1 (*High-Frequency Error Control and Prediction Stability*). *Assume the system Jacobian \mathbf{A}_k amplifies high-frequency errors, with constants $C_A \geq 1$ and $\gamma_{\text{high}} > 1$, such that for $\epsilon_{\text{high}}(t_k) = \mathbf{P}_{\text{high}} \epsilon(t_k)$:*

$$\|\mathbf{P}_{\text{high}} \mathbf{A}_k \epsilon_{\text{high}}(t_k)\| \leq C_A \gamma_{\text{high}} \|\epsilon_{\text{high}}(t_k)\|. \quad (12)$$

If a model \mathcal{F} ensures its single-step high-frequency model error is bounded by $\|\mathbf{P}_{\text{high}} \mathbf{e}_{\text{model}}(t_k)\| \leq \delta_{\text{HF}}$, then after M autoregressive steps, the accumulated high-frequency error $\epsilon_{\text{high}}(t_M)$ is bounded by:

$$\|\epsilon_{\text{high}}(t_M)\| \leq (C_A \gamma_{\text{high}})^M \|\epsilon_{\text{high}}(t_0)\| + \delta_{\text{HF}} \frac{(C_A \gamma_{\text{high}})^M - 1}{C_A \gamma_{\text{high}} - 1}, \quad (13)$$

for $C_A \gamma_{\text{high}} \neq 1$ and initial error $\epsilon_{\text{high}}(t_0)$.

Discussion of association with Turb-L1. Theorem A.1 implies that a smaller δ_{HF} (i.e., higher model accuracy for high-frequency components) is critical for mitigating error growth in systems sensitive to high-frequency perturbations ($C_A \gamma_{\text{high}} > 1$). The **Turb-L1** architecture, with its Hierarchical Dynamics Synthesis (HDS) mechanism and multi-grid components, is designed to minimize δ_{HF} by explicitly addressing *Spectral Bias* and ensuring high-fidelity information processing across scales. This architectural focus on accurately capturing high-frequency dynamics leads to a significant reduction in the model-induced error term in Eq. (13), thereby enhancing long-term stability in systems like turbulence. This provides a theoretical basis for **Turb-L1**’s observed performance in maintaining prediction fidelity over extended rollouts. Our experiments also corroborate the above viewpoint, and additional evidence is provided in the Appendix.

3 Numerical Experiments

3.1 Experiment Setup

Datasets We test **Turb-L1** on two classic datasets of two-dimensional isotropic turbulence, a canonical problem in fluid dynamics. These datasets are designed to evaluate the model’s capability to

Table 1: Performance comparison on isotropic turbulence datasets measured by L^2 error at different prediction steps. Lower L^2 error values indicate better performance.

Model Category	Datasets								
	Decaying Isotropic Turbulence					Forced Isotropic Turbulence			
	1-step	10-step	40-step	60-step	99-step	1-step	10-step	19-step	
Operator Learning Models									
✚ FNO [20] ICLR 2021	0.0267	0.3550	1.7794	2.5634	3.1284	0.0118	0.1384	1.9832	
✚ CNO [34] NEURIPS 2023	0.0407	1.7774	6.1085	7.7403	11.3015	0.0008	0.1227	1.5676	
✚ LSM [44] ICML 2023	0.0046	0.3373	3.0698	4.2579	5.1127	0.0017	0.1287	2.0382	
✚ NMO [49] KDD 2024	0.0018	0.0602	1.7634	1.9832	2.1923	0.0002	0.0043	0.1873	
Computer Vision Backbones									
📷 U-Net [35] MICCAI 2015	0.0182	0.5810	2.8367	3.7935	4.6647	0.0007	0.0296	0.6583	
📷 ResNet [12] CVPR 2016	0.0098	0.4983	1.9823	2.9983	5.8743	0.0025	0.2424	2.3630	
📷 ViT [6] ICLR 2021	0.0360	2.2588	5.4557	5.6154	5.6401	0.0074	0.2363	3.8732	
📷 DiT [30] ICCV 2023	0.0038	1.9832	2.7654	5.9862	9.9283	0.0007	0.0283	1.2731	
Spatiotemporal Models									
📺 ConvLSTM [37] NIPS 2015	0.0374	0.5643	2.2374	3.9841	4.9381	0.0443	0.0687	1.2384	
📺 SimVP [40] CVPR 2022	0.0019	0.0621	2.1104	3.8504	5.0405	0.0002	0.0046	0.2231	
📺 PastNet [48] MM 2024	0.0128	0.0415	0.5689	1.7574	2.3837	0.0073	0.0348	0.6173	
🏆 Turb-L1 Promotion	0.0002	0.0048	0.0807	0.2157	0.6171	0.0001	0.0019	0.1257	
	88.89%	92.29%	85.82%	89.13%	80.30%	50.00%	58.70%	43.66%	

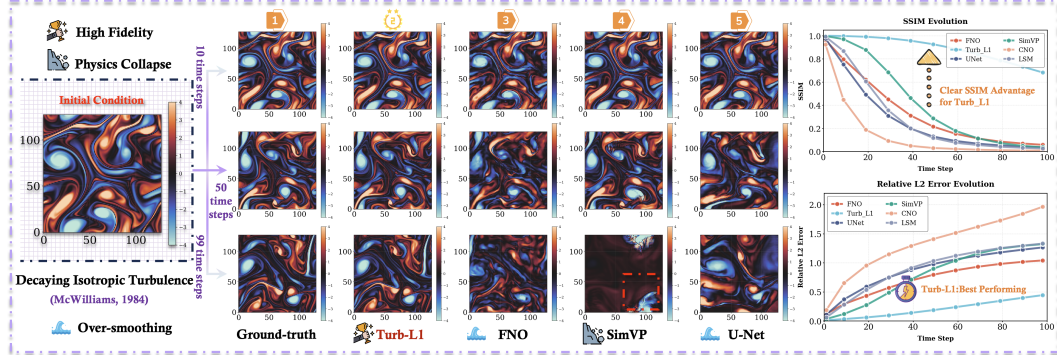


Figure 3: **Long-term prediction on 2D Decaying Isotropic Turbulence.** (Left) Initial condition. (Center Columns 1-5) Vorticity fields at $t = 10, 50, 99$ for Ground-truth, Turb-L1, FNO, SimVP, and U-Net. Turb-L1 maintains high fidelity, while FNO/U-Net show over-smoothing and SimVP (collapse icon) exhibits instability, underscoring Turb-L1’s resilience to spectral bias. (Right) Quantitative evaluation: (Top Right.) SSIM Evolution, where Turb-L1 excels in structural similarity. (Bottom Right.) Relative L^2 Error Evolution, showing Turb-L1’s superior accuracy and stability.

capture complex chaotic dynamics under different physical regimes. ✚ **Dataset I: Forced Isotropic Turbulence Benchmark.** This scenario follows the Navier-Stokes equation benchmark proposed in Li et al. [20]. The kinematic viscosity is set to $\nu = 10^{-5}$. The initial vorticity field, ω_0 , is sampled from a zero-mean Gaussian random field with a covariance operator $(-\Delta + \tau^2 I)^{-\alpha/2}$, where Δ is the Laplacian operator, I is the identity operator, and τ and α are parameters controlling the spectral shape. The energy density $E(k)$ exhibits a decay law of $E(k) \sim (k^2 + \tau^2)^{-\alpha}$. The flow is driven by a fixed, low-wavenumber external force, and no additional drag effects are considered. ✚ **Dataset II: Decaying Isotropic Turbulence (McWilliams, 1984).** [24] This scenario simulates the phenomenon of decaying turbulence. The power spectrum of the initial streamfunction, characterized by $|\hat{\psi}(\mathbf{k})|^2 \sim k^{-1}(\tau_0^2 + (k/k_0)^4)^{-1}$, where k_0 is the characteristic wavenumber and τ_0 is a spectral shape parameter, defines the initial flow field. The initial conditions facilitate a slow energy decay, and the enstrophy density evolves to exhibit features akin to a Kolmogorov energy cascade. The turbulence is unforced and evolves naturally. For more details, see the Appendix.

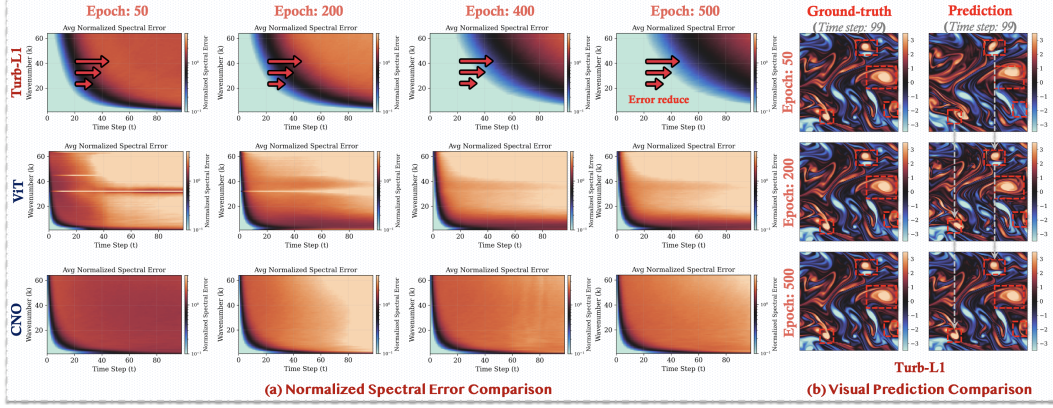


Figure 4: Evolution of spectral error and visual prediction improvement for Turb-L1 during training. (a) Normalized spectral error for Turb-L1, ViT, and CNO at different training epochs. Turb-L1 shows significantly reduced error in high-wavenumber regions with training. (b) Visual comparison of Turb-L1’s long-term predictions at early (Epoch: 50) and late (Epoch: 500) training stages, demonstrating enhanced capturing of high-frequency details and vortex structures.

Backbones To comprehensively evaluate the performance of our proposed method, we select three categories of representative deep learning models as baselines for comparison. **Operator Learning Models.** These models aim to directly learn mappings between infinite-dimensional function spaces. We choose several mainstream and cutting-edge methods from this field, including: FNO [20], CNO [34], LSM [44], and NMO [49]. **Classic Computer Vision Backbones.** These models demonstrate strong feature extraction capabilities in image processing and computer vision tasks. Specific models include: U-Net [35], ResNet [12], ViT [6], and DiT [30]. **Spatiotemporal Prediction Models.** These models are specifically designed to process and predict sequential data with temporal and spatial dependencies. Our selected representative models are: ConvLSTM [37], SimVP [40], and PastNet [48]. For more details, see the Appendix.

Experiment settings We train all models in this paper on a server equipped with eight NVIDIA A100 GPUs, each with 40GB of memory. We use the DistributedDataParallel mode from the PyTorch [29] framework for distributed training to accelerate convergence. Model inference is performed on a single NVIDIA A100 GPU. The software environment for our experiments is based on Python 3.8. We use PyTorch version 1.8.1 (CUDA 11.1), TorchVision version 0.9.1. During the training process, we consistently use the following hyperparameter configuration: the batch size is set to 20, the total number of epochs is 500, and the initial learning rate is 0.001. To ensure the reproducibility of our experiments, we fix all random seeds to 42. For more details, see the Appendix.

3.2 Main results

Table 1 presents the performance achieved across different baselines over various prediction steps. We summarize the key takeaways as follows:

Takeaway ①: Turb-L1 consistently achieves state-of-the-art performance across diverse benchmarks and prediction steps. Across both Dataset I and II, Turb-L1 achieves significantly lower L^2 errors compared to all three mainstream method categories (Operator Learning Models, Classic Computer Vision Backbones, and Spatiotemporal Prediction Models). Notably, on Dataset I, Turb-L1 demonstrates exceptional performance with an error of only 0.6171, substantially outperforming the second-best baseline NMO (2.1923). This superior performance remains consistently observable in Dataset II (0.1257 vs. 0.1873). More generally, Turb-L1 attains overall error reductions ranging from 43.66% ~ 92.29% across different prediction steps, conclusively validating our Turb-L1 effectiveness for long-term forecasting.

Takeaway ②: Turb-L1 demonstrates excellent visual fidelity and physical consistency in long-term predictions. It effectively overcomes over-smoothing and simulation collapse, issues that spectral bias causes. As Figure 3 illustrates, Turb-L1’s predictions closely match the ground truth even after 99 time steps, clearly reproducing complex vortex structures and fine flow features. This performance stems from its core Hierarchical Dynamics Synthesis mechanism, which precisely captures full-spectrum dynamic information, particularly high-frequency details. In contrast, FNO exhibits significant over-smoothing due to spectral bias and loses critical high-frequency information.

SimVP, on the other hand, experiences physics collapse from accumulated high-frequency error amplification, producing unrealistic artifacts. **Turb-L1**'s SSIM and relative L2 error curves further confirm its significant advantages in maintaining structural similarity and long-term prediction accuracy. This fully demonstrates the method's robustness and high fidelity in tracking complex multi-scale turbulence dynamics. Further ablation experiments are presented in the Appendix.

3.3 Training Dynamics: How Turb-L1 Progressively Overcomes Spectral Bias

Takeaway ③: Figure 4 shows **Turb-L1**'s progress in overcoming spectral bias and improving high-frequency prediction during training. The left plots display normalized spectral error: **Turb-L1**'s high-wavenumber error significantly decreases as epochs increase from 50 to 500, indicating its *HDS* mechanism effectively learns high-frequency details. In contrast, ViT and CNO consistently show large high-frequency errors, highlighting their limitations in overcoming spectral bias. The visual comparisons on the right confirm this: **Turb-L1** trained to Epoch 500 accurately reproduces fine vortex structures and curled edges, which are blurred at Epoch 50. This improved vortical detail capture reflects its enhanced high-frequency prediction. Thus, **Turb-L1**'s architecture-guided training effectively mitigates spectral bias, enabling high-fidelity tracking of crucial vortex dynamics.

3.4 Turb-L1's Superiority in Enstrophy Spectrum Prediction

Takeaway ④: The enstrophy spectrum analysis further reveals **Turb-L1**'s significant effectiveness in overcoming spectral bias, as illustrated in Figure 5. Compared to several baseline models, the enstrophy spectrum predicted by **Turb-L1** exhibits high consistency with the Ground Truth across the entire range, from low to high wavenumbers. Many comparative methods, such as FNO and CNO, show a significant underestimation of energy or excessive smoothing in the high-wavenumber regions, with their spectral lines falling far below the true values. This is a typical manifestation of spectral bias, where models neglect high-frequency details. In more extreme cases like SimVP, an anomalous energy accumulation even occurs in the high-frequency region, indicating the model's inability to stably handle high-frequency dynamics. In contrast, **Turb-L1** accurately captures the crucial k^{-3} energy cascade characteristic of turbulence. Its precise agreement, especially in the high-frequency part, demonstrates that it effectively learns and preserves small-scale vortex information vital for turbulence evolution, facilitated by mechanisms like Hierarchical Dynamics Synthesis. This full-spectrum, high-fidelity prediction capability is a key factor in **Turb-L1**'s ability to achieve long-term, physically consistent turbulence simulations and confirms its success in mitigating spectral bias from a frequency-domain perspective.

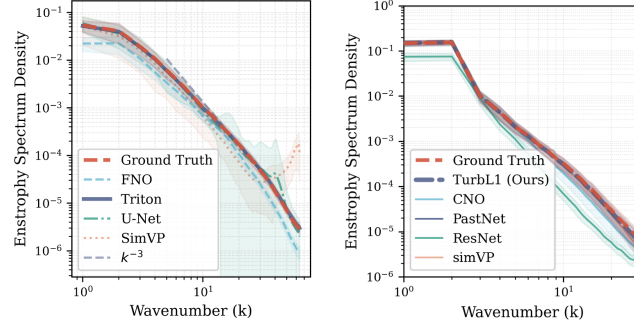


Figure 5: Comparison of enstrophy spectrum analysis. Left plot is Dataset I, Right plot is Dataset II.

4 Conclusion

In this paper, we present the first spectral bias-based analysis of the over-smoothing phenomenon in long-term turbulence prediction. Through extensive experiments, we demonstrate that existing models often overlook critical high-frequency details during training. Building on these findings, we propose **Turb-L1**, which incorporates a hierarchical dynamics synthesis mechanism within a multi-grid architecture, enabling robust and efficient long-term prediction. Extensive benchmark tests demonstrate that **Turb-L1** achieves exceptional long-term accuracy and fidelity, effectively overcoming spectral bias while preserving physical realism. We anticipate that **Turb-L1** will provide a novel perspective and a reliable framework for modeling complex dynamics in Earth systems.

References

- [1] Giancarlo Alfonsi. Reynolds-averaged navier–stokes equations for turbulence modeling. 2009.
- [2] Kaifeng Bi, Lingxi Xie, Hengheng Zhang, Xin Chen, Xiaotao Gu, and Qi Tian. Accurate medium-range global weather forecasting with 3d neural networks. *Nature*, 619(7970):533–538, 2023.
- [3] Roland Borghi. Turbulent combustion modelling. *Progress in energy and combustion science*, 14(4):245–292, 1988.
- [4] Axel Brandenburg and A Lazarian. Astrophysical hydromagnetic turbulence. *Space Science Reviews*, 178:163–200, 2013.
- [5] Peter Davidson. *Turbulence: an introduction for scientists and engineers*. Oxford university press, 2015.
- [6] Alexey Dosovitskiy, Lucas Beyer, Alexander Kolesnikov, Dirk Weissenborn, Xiaohua Zhai, Thomas Unterthiner, Mostafa Dehghani, Matthias Minderer, Georg Heigold, Sylvain Gelly, Jakob Uszkoreit, and Neil Houlsby. An image is worth 16x16 words: Transformers for image recognition at scale. In *International Conference on Learning Representations*, 2021.
- [7] Karthik Duraisamy, Gianluca Iaccarino, and Heng Xiao. Turbulence modeling in the age of data. *Annual review of fluid mechanics*, 51(1):357–377, 2019.
- [8] Zaige Fei, Fan Xu, Junyuan Mao, Yuxuan Liang, Qingsong Wen, Kun Wang, Hao Wu, and Yang Wang. Open-ck: A large multi-physics fields coupling benchmarks in combustion kinetics. In *The Thirteenth International Conference on Learning Representations*.
- [9] Yuan Gao, Hao Wu, Ruiqi Shu, Huanshuo Dong, Fan Xu, Rui Chen, Yibo Yan, Qingsong Wen, Xuming Hu, Kun Wang, et al. Oneforecast: A universal framework for global and regional weather forecasting. *arXiv preprint arXiv:2502.00338*, 2025.
- [10] Sharath S Girimaji. Partially-averaged navier-stokes model for turbulence: A reynolds-averaged navier-stokes to direct numerical simulation bridging method. 2006.
- [11] Juncal He and Jinchao Xu. Mgnet: A unified framework of multigrid and convolutional neural network. *Science china mathematics*, 62:1331–1354, 2019.
- [12] Kaiming He, Xiangyu Zhang, Shaoqing Ren, and Jian Sun. Deep residual learning for image recognition. In *Proceedings of the IEEE conference on computer vision and pattern recognition*, pages 770–778, 2016.
- [13] L Jackson, R Hallberg, and S Legg. A parameterization of shear-driven turbulence for ocean climate models. *Journal of Physical Oceanography*, 38(5):1033–1053, 2008.
- [14] Javier Jiménez. Coherent structures in wall-bounded turbulence. *Journal of Fluid Mechanics*, 842:P1, 2018.
- [15] John Kim. Control of turbulent boundary layers. *Physics of fluids*, 15(5):1093–1105, 2003.
- [16] Andreï Kolmogorov. *Turbulence: the legacy of AN Kolmogorov*. Cambridge university press, 1995.
- [17] Andrei Nikolaevich Kolmogorov. The local structure of turbulence in incompressible viscous fluid for very large reynolds numbers. *Proceedings of the Royal Society of London. Series A: Mathematical and Physical Sciences*, 434(1890):9–13, 1991.
- [18] Remi Lam, Alvaro Sanchez-Gonzalez, Matthew Willson, Peter Wirsberger, Meire Fortunato, Ferran Alet, Suman Ravuri, Timo Ewalds, Zach Eaton-Rosen, Weihua Hu, et al. Learning skillful medium-range global weather forecasting. *Science*, 382(6677):1416–1421, 2023.
- [19] Myoungkyu Lee and Robert D Moser. Direct numerical simulation of turbulent channel flow up to. *Journal of fluid mechanics*, 774:395–415, 2015.

- [20] Zongyi Li, Nikola Borislavov Kovachki, Kamyar Azizzadenesheli, Burigede liu, Kaushik Bhattacharya, Andrew Stuart, and Anima Anandkumar. Fourier neural operator for parametric partial differential equations. In *ICLR*, 2021.
- [21] Bo Liu, Jiupeng Tang, Haibo Huang, and Xi-Yun Lu. Deep learning methods for super-resolution reconstruction of turbulent flows. *Physics of fluids*, 32(2), 2020.
- [22] Miguel Liu-Schiaffini, Julius Berner, Boris Bonev, Thorsten Kurth, Kamyar Azizzadenesheli, and Anima Anandkumar. Neural operators with localized integral and differential kernels. In *ICLR 2024 Workshop on AI4DifferentialEquations In Science*, 2024.
- [23] Manuel Lopez-Martin, Soledad Le Clainche, and Belen Carro. Model-free short-term fluid dynamics estimator with a deep 3d-convolutional neural network. *Expert Systems with Applications*, 177:114924, 2021.
- [24] James C McWilliams. The emergence of isolated coherent vortices in turbulent flow. *Journal of Fluid Mechanics*, 146:21–43, 1984.
- [25] Parviz Moin and Krishnan Mahesh. Direct numerical simulation: a tool in turbulence research. *Annual review of fluid mechanics*, 30(1):539–578, 1998.
- [26] Andrei Sergeevich Monin. On the nature of turbulence. *Soviet Physics Uspekhi*, 21(5):429, 1978.
- [27] Julio M Ottino. *The kinematics of mixing: stretching, chaos, and transport*, volume 3. Cambridge university press, 1989.
- [28] Namuk Park and Songkuk Kim. How do vision transformers work? *arXiv preprint arXiv:2202.06709*, 2022.
- [29] Adam Paszke, Sam Gross, Francisco Massa, Adam Lerer, James Bradbury, Gregory Chanan, Trevor Killeen, Zeming Lin, Natalia Gimelshein, Luca Antiga, et al. Pytorch: An imperative style, high-performance deep learning library. *Advances in neural information processing systems*, 32, 2019.
- [30] William Peebles and Saining Xie. Scalable diffusion models with transformers. In *Proceedings of the IEEE/CVF international conference on computer vision*, pages 4195–4205, 2023.
- [31] Ugo Piomelli. Large-eddy simulation: achievements and challenges. *Progress in aerospace sciences*, 35(4):335–362, 1999.
- [32] Stephen B Pope. Turbulent flows. *Measurement Science and Technology*, 12(11):2020–2021, 2001.
- [33] Nasim Rahaman, Aristide Baratin, Devansh Arpit, Felix Draxler, Min Lin, Fred Hamprecht, Yoshua Bengio, and Aaron Courville. On the spectral bias of neural networks. In *International conference on machine learning*, pages 5301–5310. PMLR, 2019.
- [34] Bogdan Raonic, Roberto Molinaro, Tim De Ryck, Tobias Rohner, Francesca Bartolucci, Rima Alaifari, Siddhartha Mishra, and Emmanuel de Bézenac. Convolutional neural operators for robust and accurate learning of pdes. *Advances in Neural Information Processing Systems*, 36:77187–77200, 2023.
- [35] Olaf Ronneberger, Philipp Fischer, and Thomas Brox. U-net: Convolutional networks for biomedical image segmentation. In *Medical image computing and computer-assisted intervention–MICCAI 2015: 18th international conference, Munich, Germany, October 5–9, 2015, proceedings, part III 18*, pages 234–241. Springer, 2015.
- [36] Ruben Scardovelli and Stéphane Zaleski. Direct numerical simulation of free-surface and interfacial flow. *Annual review of fluid mechanics*, 31(1):567–603, 1999.
- [37] Xingjian Shi, Zhourong Chen, Hao Wang, Dit-Yan Yeung, Wai-Kin Wong, and Wang-chun Woo. Convolutional lstm network: A machine learning approach for precipitation nowcasting. *Advances in neural information processing systems*, 28, 2015.

- [38] Ruiqi Shu, Hao Wu, Yuan Gao, Fanghua Xu, Ruijian Gou, Wei Xiong, and Xiaomeng Huang. Advanced forecasts of global extreme marine heatwaves through a physics-guided data-driven approach. *Environmental Research Letters*, 20(4):044030, 2025.
- [39] Katepalli R Sreenivasan. Fluid turbulence. *Reviews of Modern Physics*, 71(2):S383, 1999.
- [40] Cheng Tan, Zhangyang Gao, Siyuan Li, and Stan Z Li. Simvp: Towards simple yet powerful spatiotemporal predictive learning. *arXiv preprint arXiv:2211.12509*, 2022.
- [41] Simron Thapa, Nianyi Li, and Jinwei Ye. Dynamic fluid surface reconstruction using deep neural network. In *Proceedings of the IEEE/CVF Conference on Computer Vision and Pattern Recognition*, pages 21–30, 2020.
- [42] Kun Wang, Hao Wu, Yifan Duan, Guibin Zhang, Kai Wang, Xiaojiang Peng, Yu Zheng, Yuxuan Liang, and Yang Wang. Nuwadynamics: Discovering and updating in causal spatio-temporal modeling. In *The Twelfth International Conference on Learning Representations*, 2024.
- [43] Kun Wang, Hao Wu, Guibin Zhang, Junfeng Fang, Yuxuan Liang, Yuankai Wu, Roger Zimmermann, and Yang Wang. Modeling spatio-temporal dynamical systems with neural discrete learning and levels-of-experts. *IEEE Transactions on Knowledge and Data Engineering*, 2024.
- [44] Haixu Wu, Tengge Hu, Huakun Luo, Jianmin Wang, and Mingsheng Long. Solving high-dimensional pdes with latent spectral models. *arXiv preprint arXiv:2301.12664*, 2023.
- [45] Haixu Wu, Huakun Luo, Haowen Wang, Jianmin Wang, and Mingsheng Long. Transolver: A fast transformer solver for pdes on general geometries. *arXiv preprint arXiv:2402.02366*, 2024.
- [46] Hao Wu, Yuxuan Liang, Wei Xiong, Zhengyang Zhou, Wei Huang, Shilong Wang, and Kun Wang. Earthfarsser: Versatile spatio-temporal dynamical systems modeling in one model. In *Proceedings of the AAAI Conference on Artificial Intelligence*, volume 38, pages 15906–15914, 2024.
- [47] Hao Wu, Xingjian Shi, Ziyue Huang, Penghao Zhao, Wei Xiong, Jinbao Xue, Yangyu Tao, Xiaomeng Huang, and Weiyan Wang. Beamvq: Aligning space-time forecasting model via self-training on physics-aware metrics. *arXiv preprint arXiv:2405.17051*, 2024.
- [48] Hao Wu, Fan Xu, Chong Chen, Xian-Sheng Hua, Xiao Luo, and Haixin Wang. Pastnet: Introducing physical inductive biases for spatio-temporal video prediction. In *Proceedings of the 32nd ACM International Conference on Multimedia*, pages 2917–2926, 2024.
- [49] Hao Wu, Shuyi Zhou, Xiaomeng Huang, and Wei Xiong. Neural manifold operators for learning the evolution of physical dynamics, 2024.
- [50] John C Wyngaard. *Turbulence in the Atmosphere*. Cambridge university press, 2010.
- [51] Yang Zhiyin. Large-eddy simulation: Past, present and the future. *Chinese journal of Aeronautics*, 28(1):11–24, 2015.

Supplementary materials

A	Proof of Theorem on High-Frequency Error Control	14
A.1	Preliminaries: Error Evolution Equation	14
A.2	Theorem and Proof	14
A.3	Discussion and Association with Turb-L1	15
B	Dataset Details	16
B.1	Dataset I: Forced Isotropic Turbulence	16
B.2	Dataset II: Decaying Isotropic Turbulence (McWilliams, 1984)	16
C	Metrics	17
C.1	L^2 Error	17
C.2	Structural Similarity Index Measure (SSIM)	17
C.3	Relative L^2 Error	17
C.4	Enstrophy Spectrum (Density), $E_Z(k, t)$	17
C.5	Normalized Spectral Error	18
D	Experimental Configurations	18
D.1	Configurations for Dataset I: Forced Isotropic Turbulence	18
D.1.1	Model Architectural Hyperparameters (Dataset I)	18
D.1.2	Training Configurations (Dataset I)	19
D.2	Configurations for Dataset II: Decaying Isotropic Turbulence	19
D.2.1	Model Architectural Hyperparameters (Dataset II)	19
D.2.2	Training Configurations (Dataset II)	20
E	Ablation Study	21
E.1	Ablation Study Setup for Decaying Isotropic Turbulence	21
E.1.1	Analysis of Ablation Study Results	21
E.1.2	Qualitative Analysis of Vorticity Field Predictions	23
F	Visualization of Long-Term Prediction on Forced Isotropic Turbulence	24

A Proof of Theorem on High-Frequency Error Control

This section provides a detailed proof for Theorem A.1, which establishes a bound on the accumulation of high-frequency errors in long-term autoregressive predictions.

A.1 Preliminaries: Error Evolution Equation

Let the true state evolution of a dynamical system be governed by:

$$\omega(t_{k+1}) = S(\omega(t_k)), \quad (\text{A.14})$$

where $\omega(t_k)$ is the true state at discrete time step t_k , and S is the true evolution operator. A surrogate model approximates this evolution as:

$$\hat{\omega}(t_{k+1}) = \mathcal{F}(\hat{\omega}(t_k)), \quad (\text{A.15})$$

where $\hat{\omega}(t_k)$ is the model-predicted state, and \mathcal{F} is the learned model operator.

The prediction error at time t_k is defined as $\epsilon(t_k) = \hat{\omega}(t_k) - \omega^*(t_k)$, where $\omega^*(t_k)$ denotes the true trajectory. The error at the next time step t_{k+1} is:

$$\epsilon(t_{k+1}) = \hat{\omega}(t_{k+1}) - \omega^*(t_{k+1}) \quad (\text{A.16})$$

$$= \mathcal{F}(\hat{\omega}(t_k)) - S(\omega^*(t_k)). \quad (\text{A.17})$$

Performing a first-order Taylor expansion of $\mathcal{F}(\hat{\omega}(t_k))$ around the true state $\omega^*(t_k)$, assuming $\epsilon(t_k)$ is sufficiently small:

$$\mathcal{F}(\hat{\omega}(t_k)) = \mathcal{F}(\omega^*(t_k) + \epsilon(t_k)) \approx \mathcal{F}(\omega^*(t_k)) + \nabla \mathcal{F}|_{\omega^*(t_k)} \epsilon(t_k). \quad (\text{A.18})$$

Substituting this back into the error equation:

$$\epsilon(t_{k+1}) \approx \mathcal{F}(\omega^*(t_k)) - S(\omega^*(t_k)) + \nabla \mathcal{F}|_{\omega^*(t_k)} \epsilon(t_k). \quad (\text{A.19})$$

Let $e_{\text{model}}(t_k) = \mathcal{F}(\omega^*(t_k)) - S(\omega^*(t_k))$ be the single-step model error. Assuming the Jacobian of the learned model $\nabla \mathcal{F}|_{\omega^*(t_k)}$ approximates the Jacobian of the true system $\mathbf{A}_k = \nabla S|_{\omega^*(t_k)}$, the error evolution is:

$$\epsilon(t_{k+1}) \approx \mathbf{A}_k \epsilon(t_k) + e_{\text{model}}(t_k). \quad (\text{A.20})$$

A.2 Theorem and Proof

Theorem A.1 (*High-Frequency Error Control and Prediction Stability*). Assume the system Jacobian $\mathbf{A}_k = \nabla S|_{\omega^*(t_k)}$ amplifies high-frequency errors, with constants $C_A \geq 1$ and $\gamma_{\text{high}} > 1$, such that for the high-frequency component of the error $\epsilon_{\text{high}}(t_k) = \mathbf{P}_{\text{high}} \epsilon(t_k)$ (where \mathbf{P}_{high} is the projection operator onto a high-frequency subspace):

$$\|\mathbf{P}_{\text{high}} \mathbf{A}_k \epsilon_{\text{high}}(t_k)\| \leq C_A \gamma_{\text{high}} \|\epsilon_{\text{high}}(t_k)\|. \quad (\text{A.21})$$

If a model \mathcal{F} ensures its single-step high-frequency model error is bounded by $\|\mathbf{P}_{\text{high}} e_{\text{model}}(t_k)\| \leq \delta_{\text{HF}}$, then after M autoregressive steps, the accumulated high-frequency error $\epsilon_{\text{high}}(t_M)$ is bounded by:

$$\|\epsilon_{\text{high}}(t_M)\| \leq (C_A \gamma_{\text{high}})^M \|\epsilon_{\text{high}}(t_0)\| + \delta_{\text{HF}} \frac{(C_A \gamma_{\text{high}})^M - 1}{C_A \gamma_{\text{high}} - 1}, \quad (\text{A.22})$$

for $C_A \gamma_{\text{high}} \neq 1$ and initial high-frequency error $\epsilon_{\text{high}}(t_0)$.

Proof. Let $\epsilon_{\text{high}}(t_k) = \mathbf{P}_{\text{high}} \epsilon(t_k)$ be the high-frequency component of the error at time t_k . Applying the projection operator \mathbf{P}_{high} to both sides of the error evolution equation (Eq. (A.20)):

$$\mathbf{P}_{\text{high}} \epsilon(t_{k+1}) \approx \mathbf{P}_{\text{high}} (\mathbf{A}_k \epsilon(t_k) + e_{\text{model}}(t_k)) \quad (\text{A.23})$$

$$\epsilon_{\text{high}}(t_{k+1}) \approx \mathbf{P}_{\text{high}} \mathbf{A}_k \epsilon(t_k) + \mathbf{P}_{\text{high}} e_{\text{model}}(t_k). \quad (\text{A.24})$$

Taking the norm and applying the triangle inequality:

$$\|\epsilon_{\text{high}}(t_{k+1})\| \leq \|\mathbf{P}_{\text{high}} \mathbf{A}_k \epsilon(t_k)\| + \|\mathbf{P}_{\text{high}} e_{\text{model}}(t_k)\|. \quad (\text{A.25})$$

We make the simplifying approximation that the amplification of high-frequency error is primarily driven by existing high-frequency error components, consistent with the assumption in Eq. (A.21). That is, we consider the first term on the right-hand side to be bounded in relation to $\|\epsilon_{\text{high}}(t_k)\|$:

$$\|\mathbf{P}_{\text{high}}\mathbf{A}_k\epsilon(t_k)\| \leq C_A\gamma_{\text{high}}\|\epsilon_{\text{high}}(t_k)\|. \quad (\text{A.26})$$

This step uses the assumption Eq. (A.21) by focusing on the impact of \mathbf{A}_k on the high-frequency part of $\epsilon(t_k)$, or assumes that the cross-term effects (low-frequency error contributing to high-frequency error via \mathbf{A}_k) are implicitly captured or subdominant compared to the self-amplification of high-frequency error. By the theorem's assumption, the single-step high-frequency model error is bounded:

$$\|\mathbf{P}_{\text{high}}\mathbf{e}_{\text{model}}(t_k)\| \leq \delta_{\text{HF}}. \quad (\text{A.27})$$

Substituting these bounds into Eq. (A.25), we obtain the recursive inequality for the norm of the high-frequency error:

$$\|\epsilon_{\text{high}}(t_{k+1})\| \leq C_A\gamma_{\text{high}}\|\epsilon_{\text{high}}(t_k)\| + \delta_{\text{HF}}. \quad (\text{A.28})$$

Let $G = C_A\gamma_{\text{high}}$ and $x_k = \|\epsilon_{\text{high}}(t_k)\|$. The inequality becomes:

$$x_{k+1} \leq Gx_k + \delta_{\text{HF}}. \quad (\text{A.29})$$

Unrolling this recursion for M steps:

$$\begin{aligned} x_1 &\leq Gx_0 + \delta_{\text{HF}} \\ x_2 &\leq Gx_1 + \delta_{\text{HF}} \leq G(Gx_0 + \delta_{\text{HF}}) + \delta_{\text{HF}} = G^2x_0 + (G+1)\delta_{\text{HF}} \\ &\vdots \\ x_M &\leq G^Mx_0 + (G^{M-1} + G^{M-2} + \dots + G^1 + G^0)\delta_{\text{HF}} \\ x_M &\leq G^Mx_0 + \delta_{\text{HF}} \sum_{i=0}^{M-1} G^i. \end{aligned}$$

The sum is a geometric series. Given the condition $G = C_A\gamma_{\text{high}} \neq 1$:

$$\sum_{i=0}^{M-1} G^i = \frac{G^M - 1}{G - 1}. \quad (\text{A.30})$$

Substituting this back, and replacing x_M with $\|\epsilon_{\text{high}}(t_M)\|$, x_0 with $\|\epsilon_{\text{high}}(t_0)\|$, and G with $C_A\gamma_{\text{high}}$, we arrive at the bound:

$$\|\epsilon_{\text{high}}(t_M)\| \leq (C_A\gamma_{\text{high}})^M \|\epsilon_{\text{high}}(t_0)\| + \delta_{\text{HF}} \frac{(C_A\gamma_{\text{high}})^M - 1}{C_A\gamma_{\text{high}} - 1}. \quad (\text{A.31})$$

This completes the proof of Theorem A.1. \square

A.3 Discussion and Association with Turb-L1

Theorem A.1 (Eq. (A.22)) highlights two primary sources of high-frequency error accumulation in long-term autoregressive predictions:

1. **Amplification of initial high-frequency error:** The term $(C_A\gamma_{\text{high}})^M \|\epsilon_{\text{high}}(t_0)\|$ shows that any initial high-frequency error $\|\epsilon_{\text{high}}(t_0)\|$ is amplified by the system's dynamics, characterized by $C_A\gamma_{\text{high}}$. If $C_A\gamma_{\text{high}} > 1$, this term can grow exponentially with the number of prediction steps M .
2. **Accumulation of single-step model high-frequency error:** The term $\delta_{\text{HF}} \frac{(C_A\gamma_{\text{high}})^M - 1}{C_A\gamma_{\text{high}} - 1}$ shows that the single-step high-frequency error δ_{HF} introduced by the model at each step also accumulates and is amplified by the system dynamics. This term can also grow exponentially if $C_A\gamma_{\text{high}} > 1$.

For systems like turbulence, which are inherently multi-scale and sensitive to high-frequency details (often exhibiting $C_A\gamma_{\text{high}} > 1$ due to phenomena like energy cascade and vortex stretching), controlling the growth of high-frequency error is crucial for long-term stability and fidelity. The theorem implies that minimizing the single-step high-frequency model error, δ_{HF} , is critical.

The **Turb-L1** architecture is specifically designed to address this challenge. Traditional deep learning models often suffer from *Spectral Bias*, leading to poor representation and prediction of high-frequency components, thereby resulting in a relatively large δ_{HF} . The Hierarchical Dynamics Synthesis (HDS) mechanism within **Turb-L1**, operating in a multi-grid framework, aims to:

- Explicitly capture and process high-frequency information using operators sensitive to local, high-frequency variations (e.g., convolutions with small receptive fields).
- Synthesize dynamics across different frequency bands (high, middle, and low) and then aggregate them, ensuring that high-frequency details are preserved and correctly interact with larger-scale dynamics.
- The multi-grid architecture facilitates learning across different scales, which is beneficial for representing the full spectrum of turbulent flows.

By effectively mitigating spectral bias, **Turb-L1** strives to achieve a significantly smaller δ_{HF} . According to Eq. (A.22), a smaller δ_{HF} directly leads to a slower accumulation of high-frequency error, enhancing the long-term stability and fidelity of turbulence predictions. This theoretical underpinning explains the superior performance of **Turb-L1** observed in experiments, particularly in accurately reproducing the enstrophy spectrum at high wavenumbers and maintaining structural details over extended prediction horizons.

B Dataset Details

In this work, we evaluate our proposed method, **Turb-L1**, on two canonical benchmark datasets for two-dimensional (2D) isotropic turbulence. These datasets are specifically chosen to assess the model’s capability to capture complex, chaotic fluid dynamics under different physical regimes: one with external forcing and another exhibiting natural decay. All simulations are discretized on a 128×128 uniform spatial grid.

B.1 Dataset I: Forced Isotropic Turbulence

This dataset is based on the Navier-Stokes equation benchmark introduced by Li et al. [20] in their work on Fourier Neural Operators (FNO). It simulates the evolution of vorticity in a 2D viscous, incompressible fluid on the unit torus $(0, 1)^2$. The governing equations in vorticity form are:

$$\frac{\partial w(\mathbf{x}, t)}{\partial t} + \mathbf{u}(\mathbf{x}, t) \cdot \nabla w(\mathbf{x}, t) = \nu \Delta w(\mathbf{x}, t) + f(\mathbf{x}) \quad \forall \mathbf{x} \in (0, 1)^2, t \in (0, T] \quad (\text{A.32})$$

$$\nabla \cdot \mathbf{u}(\mathbf{x}, t) = 0 \quad \forall \mathbf{x} \in (0, 1)^2, t \in [0, T] \quad (\text{A.33})$$

$$w(\mathbf{x}, 0) = w_0(\mathbf{x}) \quad \forall \mathbf{x} \in (0, 1)^2 \quad (\text{A.34})$$

where w is the vorticity field ($w = \nabla \times \mathbf{u}$), \mathbf{u} is the velocity field, w_0 is the initial vorticity field, ν is the kinematic viscosity coefficient, and $f(\mathbf{x})$ is a time-independent external forcing function.

In our study, we adopt the setup from Li et al. [20] and specifically focus on the case where the kinematic viscosity is set to $\nu = 1 \times 10^{-5}$. The initial vorticity field, w_0 , is generated by sampling from a zero-mean Gaussian random field whose covariance operator is $(-\Delta + \tau^2 I)^{-\alpha/2}$. Here, Δ denotes the Laplacian operator, I is the identity operator, and the parameters τ and α control the spectral shape, such that the initial energy spectrum density $E(k)$ follows $E(k) \sim (k^2 + \tau^2)^{-\alpha}$. The external forcing term $f(\mathbf{x})$ is a fixed force, predominantly concentrated in the low-wavenumber regime, designed to continuously inject energy into the system. No additional drag effects are considered in the simulations.

This dataset is employed to evaluate the model’s long-term prediction capabilities and its ability to capture chaotic dynamics in the presence of sustained external energy input. In the experiments presented in this paper, we extend the prediction horizon for this dataset up to 19 time steps.

B.2 Dataset II: Decaying Isotropic Turbulence (McWilliams, 1984)

This dataset simulates the classic phenomenon of 2D decaying isotropic turbulence. The setup for the initial conditions follows the seminal work by McWilliams [24], titled "The emergence of isolated

coherent vortices in turbulent flow." Unlike Dataset I, in this scenario, the fluid system evolves without any external forcing after an initial perturbation; its energy naturally decays over time.

The initial flow field is characterized by the power spectrum of its streamfunction $\psi(\mathbf{x})$. Specifically, the squared magnitude of the Fourier coefficients of the initial streamfunction, $|\hat{\psi}(\mathbf{k})|^2$ (where \mathbf{k} is the wavevector), adheres to the following spectral distribution:

$$|\hat{\psi}(\mathbf{k})|^2 \sim k^{-1}(\tau_0^2 + (k/k_0)^4)^{-1} \quad (\text{A.35})$$

where $k = |\mathbf{k}|$ is the wavenumber magnitude, k_0 is a characteristic wavenumber, and τ_0 is a parameter that shapes the spectrum. These initial conditions are designed to facilitate a slow energy decay and allow the system to self-organize into coherent vortex structures during its evolution. The enstrophy density spectrum also evolves to exhibit features akin to a Kolmogorov energy cascade.

This dataset is a crucial benchmark for evaluating a model's ability to capture long-term dynamical behavior, energy dissipation mechanisms, and the formation and evolution of complex structures (such as isolated coherent vortices) in a purely self-evolving system. In our experiments, we extend the prediction horizon for this dataset up to 99 time steps to thoroughly assess the long-term stability and fidelity of the models.

C Metrics

C.1 L^2 Error

Measures the L^2 norm of the error field, which is the difference between the predicted field ($\hat{\omega}(\cdot, t)$) and the ground truth field ($\omega(\cdot, t)$).

$$L^2 \text{ Error}(t) = \|\hat{\omega}(\cdot, t) - \omega(\cdot, t)\|_{L^2} = \sqrt{\sum_{i=1}^{N_x} \sum_{j=1}^{N_y} (\hat{\omega}_{i,j}(t) - \omega_{i,j}(t))^2} \quad (\text{A.36})$$

C.2 Structural Similarity Index Measure (SSIM)

Assesses the perceptual similarity between two fields (prediction u , ground truth v) considering local means (μ), variances (σ^2), and covariance (σ_{uv}).

$$\text{SSIM}(u, v) = \frac{(2\mu_u\mu_v + c_1)(2\sigma_{uv} + c_2)}{(\mu_u^2 + \mu_v^2 + c_1)(\sigma_u^2 + \sigma_v^2 + c_2)} \quad (\text{A.37})$$

where c_1, c_2 are stabilization constants. The overall SSIM is the mean of local SSIM values.

C.3 Relative L^2 Error

Normalizes the L^2 norm of the error field by the L^2 norm of the ground truth field.

$$\text{Relative } L^2 \text{ Error}(t) = \frac{\|\hat{\omega}(\cdot, t) - \omega(\cdot, t)\|_{L^2}}{\|\omega(\cdot, t)\|_{L^2}} = \frac{\sqrt{\sum_{i=1}^{N_x} \sum_{j=1}^{N_y} (\hat{\omega}_{i,j}(t) - \omega_{i,j}(t))^2}}{\sqrt{\sum_{i=1}^{N_x} \sum_{j=1}^{N_y} (\omega_{i,j}(t))^2}} \quad (\text{A.38})$$

C.4 Enstrophy Spectrum (Density), $E_Z(k, t)$

Describes the distribution of enstrophy (mean squared vorticity) across different wavenumbers k . Total enstrophy $Z(t) = \int_0^\infty E_Z(k, t) dk$. For 2D fields, it's computed from the Fourier transform of vorticity $\hat{\omega}(\mathbf{k}', t)$ over annular shells in Fourier space, where A is the domain area:

$$E_Z(k, t) \approx \frac{1}{\Delta k} \sum_{k \leq |\mathbf{k}'| < k + \Delta k} \frac{1}{2A} |\hat{\omega}(\mathbf{k}', t)|^2 \cdot (2\pi k') \quad (\text{A.39})$$

C.5 Normalized Spectral Error

Quantifies the relative difference between the predicted enstrophy spectrum ($E_{Z,\text{pred}}(k, t)$) and the ground truth enstrophy spectrum ($E_{Z,\text{GT}}(k, t)$) at each wavenumber k .

$$\text{Normalized Spectral Error}(k, t) = \frac{E_{Z,\text{pred}}(k, t) - E_{Z,\text{GT}}(k, t)}{E_{Z,\text{GT}}(k, t)} \quad (\text{A.40})$$

D Experimental Configurations

This section details the model hyperparameters, training procedures, data handling, and logging configurations for the experiments conducted on both datasets.

D.1 Configurations for Dataset I: Forced Isotropic Turbulence

D.1.1 Model Architectural Hyperparameters (Dataset I)

Table 2 summarizes the key architectural hyperparameters. For models with extensive parameter sets (e.g., CNO), please refer to the original publications or supplementary code.

Table 2: Architectural Hyperparameters for Dataset I (Forced Isotropic Turbulence).

Model Name	Parameter	Value(s)
Turb-L1	Input Shape (T,C,H,W)	[1, 1, 128, 128]
	Spatial Hidden Dim	128
	Output Channels	1
	Temporal Hidden Dim	256
	Num Spatial Layers	4
	Num Temporal Layers	8
FNO	Modes (modes1, modes2)	8, 8
	Width	64
	Input Channels (C_in)	1
	Output Channels (C_out)	1
SimVP	Input Shape (T,C,H,W)	[1, 1, 64, 64]
	Hidden Dim S (hid_S)	128
	Hidden Dim T (hid_T)	256
	Output Dim	1
CNO	Input Channels (in_dim)	1
	Input Size (H, W)	64, 64
	Num Layers (N_layers)	4
	Channel Multiplier	32
	Latent Lift Proj Dim	64
	Activation	'cno_lrelu'
MGNO	Num Layers	6
	Output/Input Channels	1
	Height / Width	128 / 128
LSM	Model Dim (d_model)	64
	Num Tokens / Basis	4 / 16
	Patch Size	'4,4'
U-Net	Input/Output Channels	1 / 1
	Kernel Size	3
	Dropout Rate	0.5
ResNet	Input/Output Channels	1 / 1

Continued on next page

Model Name	Parameter	Value(s)
	Dropout Rate	0.5
ViT	Image Size / Patch Size	128 / 4
	Input/Output Channels	1 / 1
	Embedding Dim / Depth	256 / 1
PastNet	Input Shape (T,C,H,W)	[1, 1, 64, 64]
	Hidden Dim T (hid_T)	256
	Inception Kernels	[3, 5, 7, 11]
ConvLSTM	Input Dim / Hidden Dims	1 / [64, 64]
	Num Layers	2
KNO	Input/Output Channels	1 / 1
	Operator Size (op_size)	64
	Modes X / Y	10 / 10

D.1.2 Training Configurations (Dataset I)

Table 3 details the training configurations. All models were trained for 500 epochs with a seed of 42.

Table 3: Training Configurations for Dataset I.

Model Name	Batch Size	Learning Rate	Parallel Method
Turb-L1	20	0.001	DistributedDataParallel
FNO	1	0.001	DataParallel
SimVP	20	0.001	DistributedDataParallel
CNO	20	0.001	DistributedDataParallel
MGNO	20	0.0005	DistributedDataParallel
LSM	20	0.001	DistributedDataParallel
U-Net	20	0.001	DistributedDataParallel
ResNet	20	0.001	DistributedDataParallel
ViT	20	0.001	DistributedDataParallel
PastNet	20	0.001	DistributedDataParallel
ConvLSTM	20	0.001	DistributedDataParallel
KNO	500	0.001	DataParallel

D.2 Configurations for Dataset II: Decaying Isotropic Turbulence

D.2.1 Model Architectural Hyperparameters (Dataset II)

Table 4 summarizes key architectural hyperparameters for Dataset II.

Table 4: Architectural Hyperparameters for Dataset II (Decaying Isotropic Turbulence).

Model Name	Parameter	Value(s)
Turb-L1	Input Shape (T,C,H,W)	[1, 1, 128, 128]
	Spatial Hidden Dim	128
	Output Channels	1
	Temporal Hidden Dim	256
	Num Spatial Layers	4
	Num Temporal Layers	8
FNO	Modes (modes1, modes2)	16, 16
	Width	64
	Input Channels (C_in)	1

Continued on next page

Table 4 – continued from previous page

Model Name	Parameter	Value(s)
	Output Channels (C_out)	1
SimVP	Input Shape (T,C,H,W)	[1, 1, 128, 128]
	Hidden Dim S (hid_S)	64
	Hidden Dim T (hid_T)	128
	Output Dim	1
CNO	Input Channels (in_dim)	1
	Input Size (H, W)	128, 128
	Num Layers (N_layers)	4
	Channel Multiplier	32
	Latent Lift Proj Dim	64
	Activation	'cno_lrelu'
MGNO	Num Layers	6
	Output/Input Channels	1
	Height / Width	128 / 128
LSM	Model Dim (d_model)	64
	Num Tokens / Basis	4 / 16
	Patch Size	'4,4'
U-Net	Input/Output Channels	1 / 1
	Kernel Size	3
	Dropout Rate	0.5
ResNet	Input/Output Channels	1 / 1
	Dropout Rate	0.5
ViT	Image Size / Patch Size	128 / 4
	Input/Output Channels	1 / 1
	Embedding Dim / Depth	256 / 1
PastNet	Input Shape (T,C,H,W)	[1, 1, 128, 128]
	Hidden Dim T (hid_T)	256
	Inception Kernels	[3, 5, 7, 11]
ConvLSTM	Input Dim / Hidden Dims	1 / [64, 64]
	Num Layers	2
KNO	Input/Output Channels	1 / 1
	Operator Size (op_size)	128
	Modes X / Y	10 / 10

D.2.2 Training Configurations (Dataset II)

Training configurations (batch size, learning rate, epochs, seed, parallel method) for Dataset II were identical to those for Dataset I (see Table 3), unless specified otherwise.

E Ablation Study

E.1 Ablation Study Setup for Decaying Isotropic Turbulence

To rigorously evaluate the contributions of the core components within our proposed **Turb-L1** architecture and to understand its mechanisms for overcoming spectral bias, we conducted a series of ablation studies on the Decaying Isotropic Turbulence benchmark dataset. This dataset, characterized by its unforced evolution and the natural emergence of a Kolmogorov-like energy cascade, provides a challenging scenario for testing long-term prediction fidelity, particularly concerning the preservation of fine-scale vortex structures and high-frequency dynamics.

Our ablation analysis focuses on dissecting the impact of the two primary architectural innovations in **Turb-L1**: the Hierarchical Dynamics Synthesis (HDS) mechanism and the Multi-Grid (MG) framework. Additionally, we explore the model’s ability to leverage information across the frequency spectrum by creating variants that are restricted to primarily processing either high-frequency or low-frequency components.

The following ablated versions of **Turb-L1** were designed and evaluated:

1. **Turb-L1 w/o HDS (Without Hierarchical Dynamics Synthesis):** In this variant, the core HDS module is entirely removed from the **Turb-L1** architecture. The multi-grid encoder and decoder structures are retained, and a baseline dynamics evolution module (e.g., a stack of three standard convolutional layers) replaces the HDS mechanism. This setup aims to quantify the direct impact of the explicit multi-frequency synthesis performed by HDS.
2. **Turb-L1 w/o MG (Without Multi-Grid Architecture):** This variant removes the multi-grid projection and prolongation operators from both the encoder and decoder. The model operates on a single, fixed-resolution latent space. The HDS mechanism, however, is retained and adapted to function within this single-grid framework. This configuration is designed to isolate the benefits derived from the hierarchical, multi-scale processing enabled by the MG architecture.
3. **Turb-L1 (High-Freq Only Path in HDS):** To assess the model’s reliance on high-frequency information, we modified the HDS module within the full **Turb-L1** (including MG). Specifically, the pathways responsible for processing low and middle-frequency dynamic primitives within HDS (i.e., \mathcal{T}_{ω_L} and \mathcal{T}_{ω_M} as described in Section 2.4) are disabled. The model is thus forced to primarily rely on the high-frequency synthesis path (i.e., \mathcal{T}_{ω_H}) for evolving the turbulent state.
4. **Turb-L1 (Low-Freq Only Path in HDS):** Complementary to the "High-Freq Only" variant, this setup modifies the HDS module to predominantly utilize the low-frequency synthesis pathway (i.e., \mathcal{T}_{ω_L}). The high and middle-frequency pathways are disabled, compelling the model to base its predictions primarily on the evolution of large-scale, low-frequency structures.

For all ablation variants, the training procedure, including hyperparameters, loss functions, and the number of training epochs, was kept consistent with the training of the full **Turb-L1** model to ensure a fair comparison.

E.1.1 Analysis of Ablation Study Results

The effectiveness of the core components within **Turb-L1**, namely the Hierarchical Dynamics Synthesis (HDS) mechanism and the Multi-Grid (MG) architecture, was further investigated through a comprehensive ablation study. The results, presented in Figure 6 (training and validation losses) and Figure 7 (long-term MSE and SSIM), provide clear insights into the contribution of each component.

Critical Role of Hierarchical Dynamics Synthesis (HDS). The HDS mechanism stands out as the most critical component for the model’s performance. As shown in Figure 6, the variant ‘w/o HDS’ (model without HDS, dark blue curve in loss plots) exhibited by far the highest training and validation losses, saturating at approximately $5 \times 10^{-3} - 10^{-2}$. This poor learning capability translated directly into dismal long-term prediction accuracy (Figure 7, teal curve for ‘w/o HDS’): its MSE rapidly escalated beyond 5.0, and its SSIM plummeted to near zero within a few time steps. This starkly contrasts with variants incorporating HDS. This underscores that the explicit, multi-path synthesis

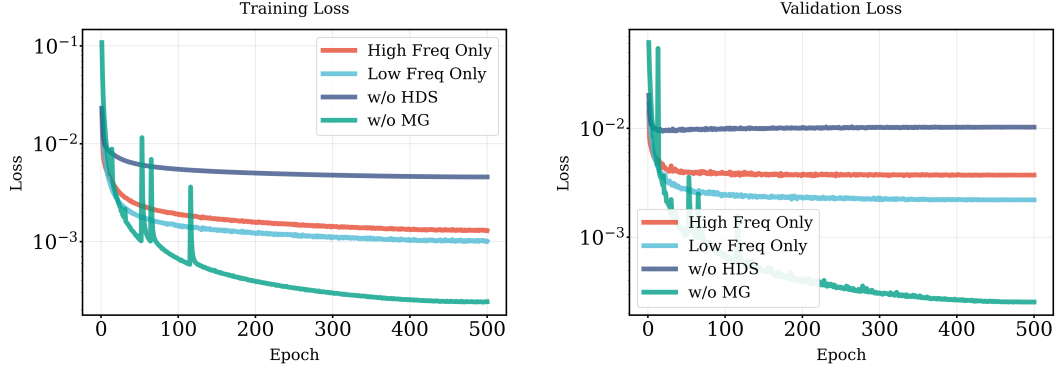


Figure 6: Training and validation loss curves for different ablation variants of **Turb-L1** on the Decaying Isotropic Turbulence dataset over 500 epochs. **(Left)** Training loss. **(Right)** Validation loss. The legend indicates: ‘High Freq Only’ (model primarily processing high-frequency components), ‘Low Freq Only’ (model primarily processing low-frequency components), ‘w/o HDS’ (model without the Hierarchical Dynamics Synthesis mechanism), and ‘w/o MG’ (model without the Multi-Grid architecture but retaining HDS). The ‘w/o HDS’ variant exhibits the highest loss, highlighting the critical role of the HDS mechanism. The ‘w/o MG’ variant, which retains HDS, achieves the lowest loss among the depicted ablated models. The y-axis is on a logarithmic scale.

of dynamics across different frequency scales, as performed by HDS, is indispensable for learning the complex, multi-scale nature of turbulence and for overcoming the spectral bias that plagues conventional architectures.

Contribution of the Multi-Grid (MG) Architecture. The ‘w/o MG’ variant (model with HDS but without the MG architecture, teal curve in Figure 6, light purple curve in Figure 7) demonstrated the best performance among all ablated models shown in the figures. Its training and validation losses were the lowest (Figure 6), and it achieved significantly superior long-term prediction stability, maintaining an MSE around 0.5-0.6 and an SSIM around 0.7 even at $t = 100$ (Figure 7). While the full **Turb-L1** model (which includes both HDS and MG, and whose performance surpasses this ‘w/o MG’ variant) is not depicted in these specific ablation comparison figures, the strong performance of the ‘w/o MG’ variant itself highlights the robustness conferred by the HDS mechanism. The further improvement achieved by the full **Turb-L1** indicates that the MG architecture provides an additional synergistic benefit by facilitating more effective hierarchical feature extraction and cross-scale interaction modeling, thereby enhancing the overall predictive capabilities of the HDS module.

Necessity of Full-Spectrum Information Processing. The variants ‘High Freq Only’ and ‘Low Freq Only’ (processing predominantly high or low-frequency components, respectively) both showed substantially poorer performance than the ‘w/o MG’ variant (which processes the full spectrum via HDS). In Figure 6, their losses saturated at higher levels (orange-red and light blue curves). More critically, their long-term prediction fidelity was severely compromised (Figure 7, pink and olive green curves), with high MSE values and SSIM scores rapidly decaying to zero. The ‘Low Freq Only’ variant performed marginally better than the ‘High Freq Only’ variant in terms of loss and long-term metrics, suggesting that large-scale structures might be somewhat easier to capture or contribute more to these aggregate error metrics in decaying turbulence. However, neither approach was sufficient. This confirms that accurately predicting turbulence evolution necessitates a model capable of capturing and synthesizing information across the entire frequency spectrum, a capability central to the design of our HDS mechanism.

In summary, these ablation studies validate our architectural choices. The HDS mechanism is paramount for achieving high-fidelity turbulence prediction by explicitly addressing spectral bias. The MG architecture further refines this by enabling effective multi-scale processing. Furthermore, the results underscore the inadequacy of models restricted to narrow frequency bands, reinforcing the need for a holistic, full-spectrum approach as embodied by **Turb-L1**.

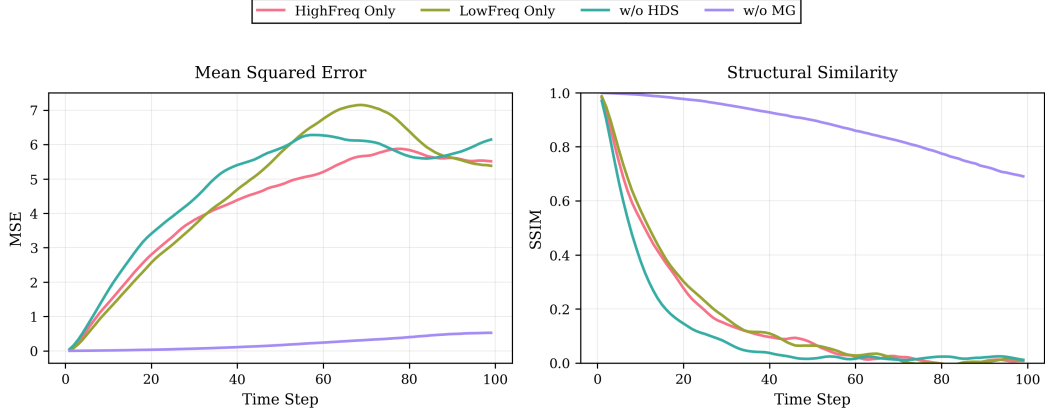


Figure 7: Long-term prediction performance of **Turb-L1** ablation variants on the Decaying Isotropic Turbulence dataset, evaluated up to 100 time steps. **(Left)** Mean Squared Error (MSE) over time. **(Right)** Structural Similarity (SSIM) over time. The legend (top) shows: ‘HighFreq Only’ (pink), ‘LowFreq Only’ (olive green), ‘w/o HDS’ (teal), and ‘w/o MG’ (light purple). The ‘w/o MG’ variant (light purple), which retains the HDS mechanism but lacks the multi-grid architecture, demonstrates significantly superior long-term stability with the lowest MSE and highest SSIM compared to other ablated versions shown. Variants without HDS or relying on single frequency bands exhibit rapid performance degradation.

E.1.2 Qualitative Analysis of Vorticity Field Predictions

Beyond quantitative metrics, we qualitatively assessed the performance of the ablated **Turb-L1** variants by visualizing their predicted vorticity fields over an extended period, as depicted in Figure 8. This visual inspection provides crucial insights into how well each model captures the intricate dynamics and preserves the physical realism of decaying turbulence.

The Ground Truth (top row) illustrates the complex evolution of turbulent eddies, characterized by stretching, merging, and filamentation, with a rich spectrum of scales. The ‘w/o MG’ variant (bottom row), which retains the HDS mechanism, demonstrates a remarkable ability to track these complex dynamics. Its predicted fields maintain a high degree of structural similarity to the Ground Truth throughout the entire simulation up to $t = 88$. Fine-scale vortex filaments and the overall morphology of larger eddies are well-preserved, indicating that the HDS mechanism effectively captures cross-scale interactions and mitigates excessive numerical dissipation or smoothing often seen in long-term autoregressive predictions.

In stark contrast, the ‘w/o HDS’ variant (fourth row) completely fails to produce physically plausible results. From early time steps, its predictions deviate significantly, and by $t = 22$ and beyond, the fields degenerate into non-physical, patchy structures, bearing no resemblance to the true turbulent flow. This visually confirms the findings from the loss and error metrics: the HDS mechanism is absolutely fundamental for learning the underlying physics.

The ‘HighFreq Only’ (second row) and ‘LowFreq Only’ (third row) variants also exhibit significant deficiencies. While the ‘HighFreq Only’ model initially captures some smaller-scale features, it progressively loses coherence and energy, leading to an overly smoothed field by $t = 55$. The ‘LowFreq Only’ model, from the outset, fails to resolve fine-scale structures, resulting in a blurry and overly diffuse representation of the vorticity field. As time progresses, it loses almost all small-scale information, retaining only vague, large-scale outlines that deviate substantially from the Ground Truth. These observations underscore the necessity of a full-spectrum approach, as models focusing on limited frequency bands cannot sustain high-fidelity predictions of the multi-scale turbulent cascade.

These qualitative results strongly corroborate our quantitative findings and further highlight the efficacy of the HDS mechanism in **Turb-L1**. Even without the multi-grid framework, HDS enables robust and physically consistent long-term tracking of turbulence evolution, a feat that other ablated versions are unable to achieve. The superior performance of the full **Turb-L1** model would build

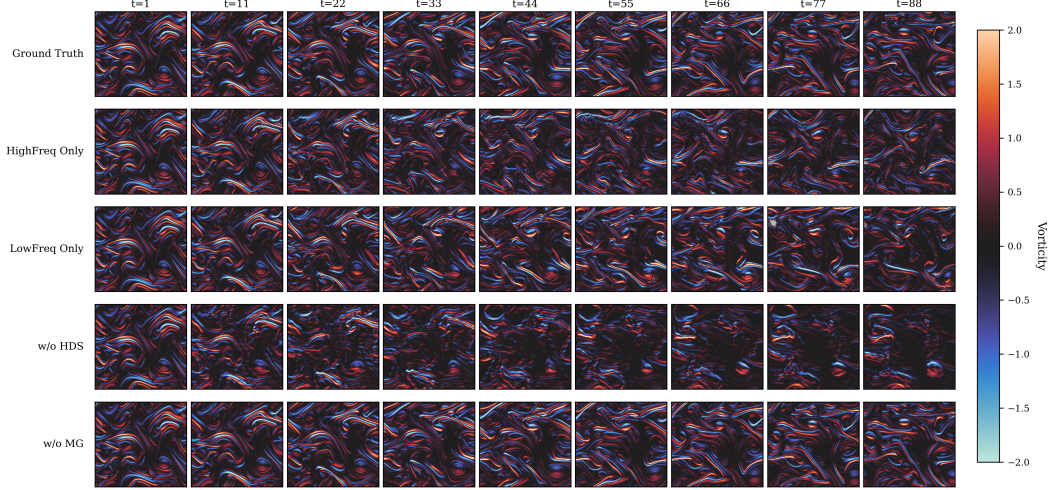


Figure 8: Visual comparison of predicted vorticity fields (ω) by different ablation variants of **Turb-L1** against the Ground Truth for Decaying Isotropic Turbulence. Snapshots are shown at nine time instances from $t = 1$ to $t = 88$. Rows display results from: Ground Truth, ‘HighFreq Only’, ‘LowFreq Only’, ‘w/o HDS’ (without Hierarchical Dynamics Synthesis), and ‘w/o MG’ (with HDS but without Multi-Grid architecture). The ‘w/o MG’ variant qualitatively best reproduces the evolution of turbulent structures and maintains high fidelity to the Ground Truth over extended periods, significantly outperforming other ablated models. The ‘w/o HDS’ variant fails to capture any physically realistic dynamics, while ‘HighFreq Only’ and ‘LowFreq Only’ variants exhibit excessive smoothing and loss of fine-scale details over time.

upon this strong foundation laid by HDS, with the MG architecture further enhancing the resolution of fine-scale details and the accuracy of cross-scale energy transfer.

F Visualization of Long-Term Prediction on Forced Isotropic Turbulence

To further demonstrate the robustness and superior long-term prediction capabilities of **Turb-L1**, we present a qualitative comparison against several baseline methods on the Forced Isotropic Turbulence benchmark. This benchmark involves continuously forced dynamics, posing a distinct challenge compared to decaying turbulence as the model must accurately capture both the externally driven evolution and the internal turbulent cascade. Figure 9 displays the predicted vorticity fields from an initial condition up to $t = 19$.

As illustrated, **Turb-L1** (**Turb-L1**, second row) consistently generates predictions that closely mirror the ground truth evolution (approximated by the first row’s sequence after the initial condition). Even at later stages like $t = 17$ and $t = 19$, **Turb-L1** successfully preserves the sharpness of vortex edges, the intricate details of smaller eddies, and the overall complex topology of the turbulent flow. This high degree of visual fidelity indicates **Turb-L1**’s effectiveness in maintaining spectral accuracy across a wide range of wavenumbers and its ability to handle the non-linear interactions inherent in forced turbulence.

In contrast, all baseline methods exhibit noticeable degradation over time. Convolutional Neural Operators (CNO, third row) and PastNet (fourth row) begin to show signs of excessive smoothing and loss of fine-scale details from intermediate time steps (around $t = 7$ to $t = 11$). By $t = 19$, their predictions, while retaining some large-scale features, lack the rich high-frequency content present in the ground truth and **Turb-L1**’s output. ResNet (fifth row) displays even more pronounced smoothing artifacts from earlier on, failing to capture the strength and definition of many vortical structures. SimVP (sixth row) also struggles with long-term fidelity, its predictions becoming progressively blurred and distorted, losing critical structural information.

These visual results on the forced turbulence scenario reinforce the conclusions drawn from the decaying turbulence experiments and quantitative metrics. The inherent spectral bias in many

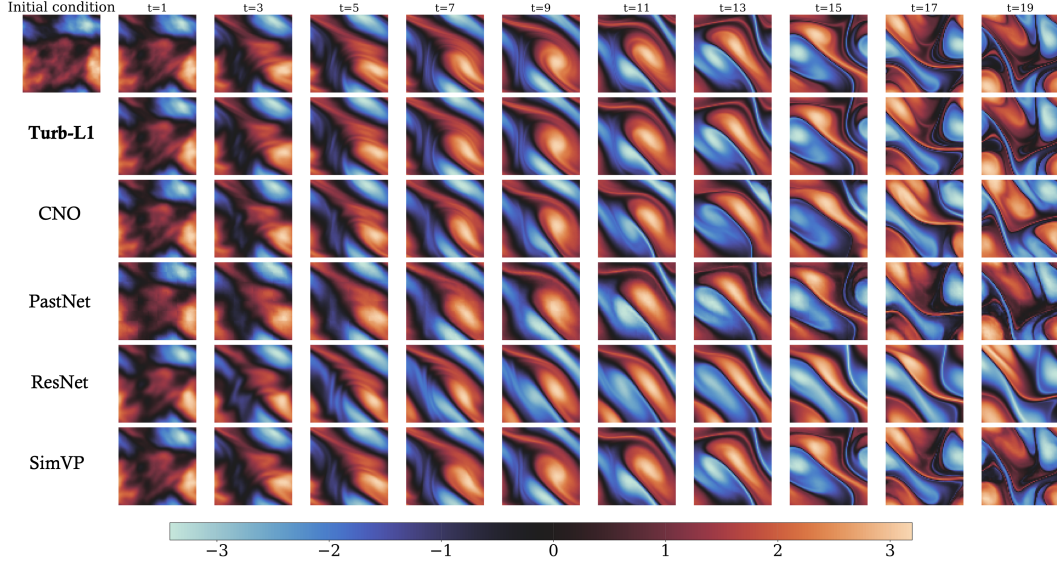


Figure 9: Qualitative comparison of vorticity field (ω) predictions for Forced Isotropic Turbulence by **Turb-L1** (Turb-L1) and baseline methods. The first row displays the initial condition and subsequent snapshots representing the ground truth evolution. Predictions are shown for time steps $t = 1, 3, \dots, 19$. **Turb-L1** maintains high fidelity to the ground truth evolution, accurately capturing fine-scale structures and complex interactions throughout the sequence. In contrast, baseline methods such as CNO, PastNet, ResNet, and SimVP exhibit varying degrees of excessive smoothing, loss of high-frequency details, and structural distortions, particularly at later time steps. This visualization further underscores the capability of **Turb-L1** to overcome spectral bias and achieve robust long-term turbulence forecasting.

conventional deep learning architectures, including those designed for spatiotemporal forecasting or operator learning, limits their ability to perform accurate, high-fidelity, long-range predictions of complex fluid dynamics. **Turb-L1**, with its explicit mechanisms for hierarchical dynamics synthesis and overcoming spectral bias, demonstrates a clear advantage in robustly tracking the full evolution of turbulence under continuous forcing, making it a promising approach for practical scientific and engineering applications requiring reliable long-term forecasting.